30 months data set of glider physico-chemical data off Mayotte Island near the Fani Maoré volcano

Alexandre Heumann[1,2], Félix Margirier[1], Emmanuel Rinnert[2], Pascale Lherminier[3], Carla Scalabrin[2], Louis Géli[2], Orens Pasqueron de Formmervault[4], and Laurent Béguery[1]

[1]ALSEAMAR, Rousset, France
[2]Geo-Ocean UMR 6538 CNRS - Ifremer - UBO, Plouzané, France
[3]LOPS UMR 6523 CNRS - Ifremer - UBO - IRD, Plouzané, France
[4]OceanOPS, World Meteorological Organization / Intergovernmental Oceanographic Commission (IOC) of UNESCO, Monaco

Correspondence: Alexandre Heumann (aheumann@alseamar-alcen.com)

Abstract. In May 2018, an unprecedented long and intense seismic-volcanic crisis broke out off the island of Mayotte (Indian Ocean) and was associated with the birth of an underwater volcano (Fani Maoré). Since then, an integrated observation network has been created (REVOSIMA), with the objective of monitoring and better understanding underwater volcanic phenomena. Recently, an autonomous ocean glider (ALSEAMAR's SeaExplorer) has been deployed to supplement the data obtained during a series of oceanographic surveys (MAYOBS) carried out on an annual basis. Operated by ALSEAMAR in collaboration with IFREMER, the glider performed a continuous monitoring of 30 months of the water column between September 2021 and April 2024 from the sea surface to 1,250 meters water depth with the objective to acquire hydrological properties, water currents and dissolved gas concentrations. This monitoring showed the feasibility and value to measure autonomously, continuously and at a high spatio-temporal scale, physical (temperature, salinity, ocean current) and biogeochemical parameters (O_2, CH_4, CO_2, bubbles/droplets, vertical speed anomalies related to droplets) over several months from a glider. In particular, innovating sensing capabilities (e.g., MINICO2, ADCP) have shown great potential in the context of the Mayotte seismic volcano crisis, despite technical challenges (complex algorithms, sensor capabilities, etc.).

1 Introduction

Mayotte is a French overseas territory, part of the volcanic archipelago of the Comoros Islands, northwest of Madagascar. It was last volcanically active on land less than 7,000 years ago (Zinke *et al.*, 2003; 2005).

On May 10, 2018, a seismic-volcanic crisis of unprecedented intensity and duration began off the two main islands of Grande-Terre and Petite-Terre (Lemoine *et al.*, 2020). More than 11,000 earthquakes were recorded, up to a magnitude of 5.9, in an area where only two seismic events had been recorded since 1972 (Feuillet *et al.*, 2021). At sea, the epicenters of these earthquakes were divided into the Proximal area (5 to 15 km east of Petite-Terre) and Distal area (25 km east of Petite-Terre).

Following the start of this seismic crisis on July 1, 2018, surface displacements were measured by the GPS stations present in Mayotte, revealing an eastward displacement of between 21 and 25 cm for all these stations, as well as a subsidence of between

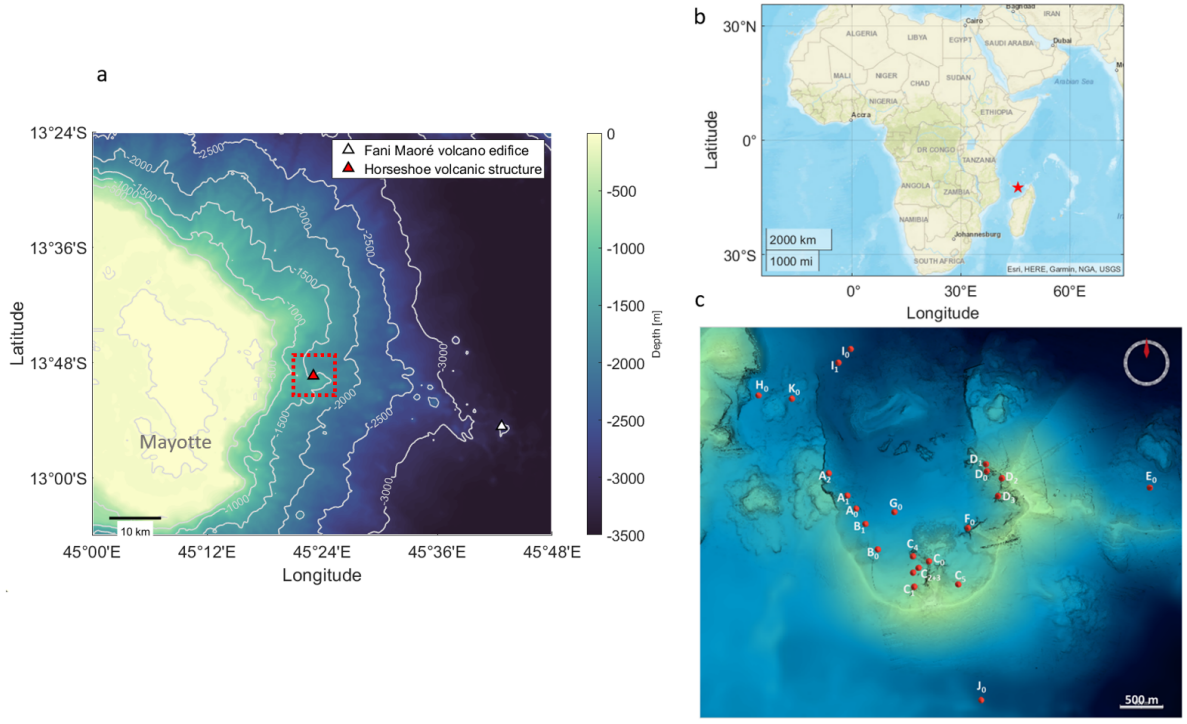

Figure 1. Map view of Mayotte (a); the Fani Maoré volcano edifice is represented by the white triangle which lies 50 km southeast of Mayotte and the Horseshoe area is represented by the red triangle and the red dotted line located 10 km east of Mayotte. Map view of Africa and Middle East (b) where the red star is the Mayotte Island. Map illustrating the Horseshoe structure (c). The red dots correspond to the discovered emission sites of magmatic fluid identified with the multibeam echosounder during the REVOSIMA MAYOBS cruises (https://doi.org//10.12770/070818f6-6520-49e4-bafd-9d4d0609bf7d) and validated by in situ visual observations with the ROV VICTOR during the GEOFLAMME cruise (DOI 10.17600/18001297). Bathymetric data were provided with a resolution of 20 m (https://doi.org/10.18142/291).

10 and 19 cm depending on their location (Feuillet *et al.*, 2021).

In response to this crisis, French laboratories and institutions (Institut de Physique du Globe de Paris (IPGP), Centre National de la Recherche Scientifique (CNRS), Bureau de Recherches Géologiques et Minières (BRGM), Institut Français de Recherche pour l'Exploitation de la Mer (IFREMER), Institut de Physique du Globe de Strasbourg (IPGS)) created a volcanological and seismological monitoring network in Mayotte, the Réseau de surveillance volcanologique et sismologique de Mayotte (REVOSIMA, http://www.ipgp.fr/fr/revosima/acteurs-reseau). This marine and terrestrial observatory, both marine and terrestrial, benefits from the financial support of several ministries (Ministry of Overseas, Ministry of the Interior, Ministry of Higher Education, Research and Innovation, Ministry of Ecological Transition and Solidarity) and aims to further our understanding of the seismic-volcanic activity for preservative measures in order to protect populations. As part of REVOSIMA, several oceanographic cruises have been carried out (MAYOBS cruises, https://doi.org/10.18142/291) and bulletins monitoring seismo-volcanic activity are published monthly (http://www.ipgp.fr/fr/revosima/actualites-reseau). The first oceanographic

cruise (MAYOBS1) was carried out from May 02 to 18, 2019 on the RV *Marion Dufresne*, and led to the discovery of the on-going eruption of the new Fani Maoré submarine volcano. A new volcanic structure of 800 m formed during this crisis with a height of around 800 m, located 50 km off the coast of Mayotte, at a depth of 3,500 m (Feuillet *et al.*, 2021, Aiken *et al.*, 2021, Fig. 1). The estimated volume of magma emitted during this eruptive period is $6.55\ km^3$, ranking this event as the largest submarine volcanic eruption ever documented (Feuillet *et al.*, 2021). Four other on-going lava flows were revealed during subsequent oceanographic cruises in the nearby area around the new volcano (Feuillet *et al*, 2021.). During the MAYOBS cruises, the Horseshoe preexisting volcanic structure, located above the Proximal swarm at an average seafloor depth of 1,400 m, was a particular area of interest (Fig. 1). Acoustic plumes and geochemical anomalies (elevated concentrations of dissolved gases such as carbon dioxide CO_2, methane CH_4 and dihydrogen H_2) were detected using a multibeam echo-sounder and CTD rosette measurements. These acoustic plumes are detectable in the water column from the seafloor up to around 500 m and are distributed over 23 active emission sites identified to date (Scalabrin, 2023; Fig. 1). The specific magmatic origin of these fluid emissions has yet to be determined (Mastin *et al.*, 2023).

The ocean circulation around the Mayotte island is mainly influenced by the instabilities of Northeast Madagascar Current (NEMC) which originates from the splitting of the westward South Equatorial Current (SEC) (Schott *et al.*, 2009). While the anticyclonic eddies, mainly generated west of Cape Amber (the northernmost cape of Madagascar), strongly influence the circulation around Mayotte island, cyclonic eddies formed along the northwest coast of Madagascar rarely reach the island (Collins *et al.*, 2014). The large-scale circulation is also strongly influenced by seasonally reversing winds linked to the monsoon regimes (Manyilizu *et al.*, 2016).

This highly complex circulation consists of a southward flow coupled with mesoscale eddies (diameter $\geq$ 300 km) that can affect the entire water column (de Ruijter *et al.*, 2002; Halo *et al.*, 2014). The general circulation in the area is even more complex due to the significant influence of the islands on the local hydrodynamic context.

Significant variability in hydrographic parameters is observed within the upper 1,500 m of the water column. This temporal variability spans a broad range of timescales. High-frequency variations (from a few hours to several days) are primarily driven by tidal forcing. At intermediate timescales, fluctuations with periodicity of 60 to 90 days are associated with the passage of anticyclonic eddies, particularly in the southern part of the study area (Collins *et al.*, 2014). On longer timescales, annual variability is evident and is largely governed by large-scale climatic forcing.

Relatively little reference data is available for the near area of the Mayotte Island and it remains poorly understood. Tide gauges have been installed on the coasts of the main islands, and internal tidal waves have been observed during MAYOBS campaigns. In order to monitor the dissolved gas dynamics related to volcanic events in the Horseshoe area and as a complement to regular oceanographic cruises, SeaExplorer glider deployments from ALSEAMAR (https://www.alseamar-alcen.com/) equipped with biogeochemical sensors are carried out since September 17, 2021 with funding from REVOSIMA. These deployments are still carried out up to date to ensure the monitoring of this seismo-volcanic crisis.

The SeaExplorer glider is a member of the family of autonomous underwater drones that can provide continuous collection of high-resolution underwater data between the surface and its maximum depth rating (1,250 m) over very wide spatial (several thousand kilometers) and temporal (up to two months) coverage. Supervised by an Iridium satellite link, the vehicle enables

near-real-time observation and monitoring of the oceans from a control center on land. The Global Ocean Observing System (GOOS), led by the Intergovernmental Oceanographic Commission (IOC) of UNESCO, and co-sponsored by the World Meteorological Organization (WMO), the United Nations Environment Programme (UNEP) and the International Science Council (ISC), has been coordinating national ocean observing efforts for more than 20 years. In this international effort, the role of autonomous glider observations has always been seen as a way to compensate for the limitations of other observing means (Stommel, 1989). The contribution of gliders began in earnest in the 2010s, when the technology was mature enough to contribute to global observations (Testor *et al.*, 2010). Since 2016, the OceanGliders component of GOOS has also been in charge of the coordination and improvement of the use of gliders around the world.

2 Data and Methods

2.1 Mission overview

The glider has been deployed at sea near the eastern coast of Petite-Terre since September 17, 2021 (12 km southwest of the Horseshoe area 12°53.5', 45°19' E). It is operated for 14 days on average before being recovered at sea to collect the full data set. The glider is then immobilized on land for one night to recharge the battery and perform regular maintenance before being redeployed the next day.

In the course of more than two and a half years of deployment, six gliders have been used for 72 deployments (see Appendix A table A1).

These gliders are equipped with a CTD (conductivity, temperature, depth), either a SeaBird's GPCTD or a RBR's LEGATO. Dissolved oxygen sensors are also deployed, an SBE43F from SeaBird coupled with the GPCTD and an AROD-FT from JFE coupled with the LEGATO. These two sets of sensors, while having small technology differences (pumped sensors for SeaBird and unpumped sensors for RBR and JFE), provide comparable data (see Appendix D table D1). The scientific payload also includes an 1MHz ADCP from Nortek (Signature1000 ADCP specifications with a casing modified for glider integration), a METS (dissolved methane sensor) from Franatech and a MINICO2 (dissolved CO_2 sensor) from Pro-Oceanus (see Appendix A table A1).

To carry out the mission, a specific and unusual sampling strategy was implemented. Until August 2023, the glider was limited to its maximum immersion depth of 1,000 m. In order to stay as near as possible to the seafloor where magmatic fluid emissions occur and should be sampled, the glider's navigation consisted in a 3-phase progression : a downward phase where the glider reached a depth of 1,000 m; a forward navigation phase, with about ten ascent/descent phases (i.e. yo) between 900 and 1,000 m; and a final phase of ascent to the surface. Dives carried out in the Horseshoe area last on average 8 to 9 hours , with 6 hours on average between 900 and 1,000 m, covering a distance of around 6 km. This radial navigation strategy, consisting on a navigation at fixed heading toward the central point of the Horseshoe structure, enables objective sampling of the zone of interest, covering all its quadrants equally, with maximum sampling effort at its center, decreasing progressively with distance (Fig. 2).

For the first time, two glider prototypes with a maximum immersion capacity of 1,250 m have also been deployed in the area

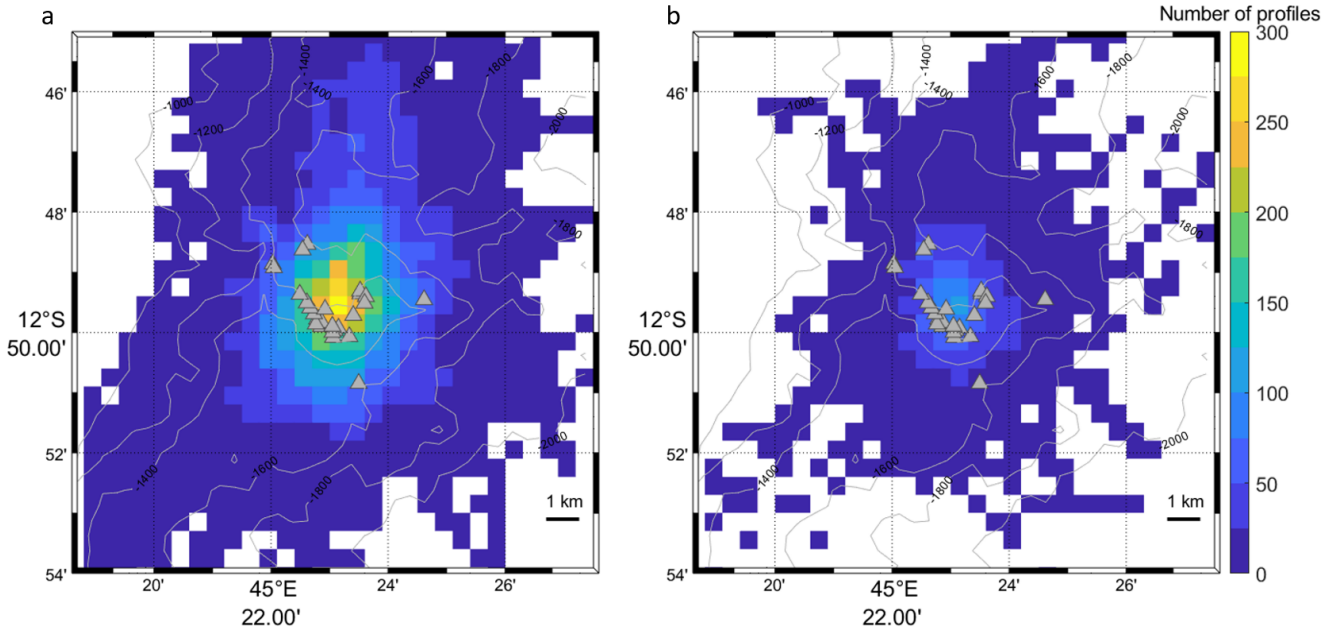

Figure 2. Map illustrating the sampling effort based on the number of profiles acquired with the 1,000 m max depth rating SeaExplorer between September 2021 and August 2023 in rectangles of 0.25 km^2 (a) and map illustrating the sampling effort based on the number of profiles acquired by the 1,250 m max depth rating SeaExplorer between August 2023 and April 2024 in rectangles of 0.25 km^2 (b). The triangles are the active fluid emission sites identified with the multibeam echosounder during the REVOSIMA MAYOBS cruises (DOI 10.12770/070818f6-6520-49e4-bafd-9d4d0609bf7d) and validated by *in situ* visual observations with the ROV VICTOR during the GEOFLAMME cruise (DOI 10.17600/18001297). Isobaths are processed from GEBCO gridded bathymetry data (DOI 10.5285/1c44ce99-0a0d-5f4f-e063-7086abc0ea0f).

since August 2023. A slightly different navigation method was chosen, opting for spirals instead of straight forward dives. The radius of these spirals is 1.5 km, in order to cover the entire study area as nearly as possible over the duration of a deployment. Initially, a wide mapping of the area has been chosen until August 2023 to detect seafloor fluid emissions and get an idea of the physico-chemical properties over a large area. With this new navigation method, sampling is then focused on better characterization of the active fluid sites (Fig. 2).

These spirals also consist of a downward phase to a depth of 1,250 m, followed by several yos between 800 and 1,250 m, and finally an ascent to the surface. These types of dives last an average of 10 hours. This sampling method was chosen to ensure the good quality of data from dissolved gas sensors by flushing the sensors (see Sections 2.2.2 and 2.2.3) and to focus the navigation on known active sites and their immediate surroundings.

The data produced during the continuous acquisition at high sample rates between September 2021 and April 2024 represents a substantial amount ($\sim$ 2.2 million measuring points per sensor corresponding to $\sim$ 22,000 dives).

2.2 Data processing

The CTD and dissolved gas sensors mounted on the SeaExplorer glider acquire measurements at a frequency of 1 Hz, subsequently averaged into 30-second time series available through the SEANOE data center (see Data availability). While data are averaged to 30-second intervals, this corresponds to approximately 5 meters of vertical resolution at a typical glider ascent or descent speed. To optimize power consumption, the ADCP operates at a lower sampling frequency of 0.1 Hz, with its data similarly averaged into 30-second intervals. As a result, fine-scale vertical structures or sharp shear zones may be partially smoothed, although the resolution remains adequate for capturing broader vertical patterns of current variability.

2.2.1 CTD and DO data

For the sensor pair GPCTD and SBE43F processing, the salinity (SAL) is derived from raw conductivity measurements and the potential density with reference pressure of 0 dbar is approximated with the 75-term function of temperature (TEMP), salinity and pressure (PRES) (Roquet *et al.*, 2015). Computations were performed according to international standards and using TEOS-10 GOOS standards (http://www.teos-10.org/pubs/IOC-XXV-3_e.pdf).

Data processing is carried out in accordance with OceanGliders SOPs (Lopez-Garcia *et al.*, 2022, https://github.com/OceanGlidersCommunity). Moreover, the thermal lag effect was addressed using the methodology described in Garau *et al.*, 2011 for both CTD sensors.

Computation of dissolved oxygen data in physical units was performed following Owens and Millard, 1985 algorithm.

For the sensor pair LEGATO CTD and AROD-FT, the data are processed internally by the sensors. Dissolved oxygen data are directly available in $\mu mol/kg$ while salinity data is also computed from the conductivity data using the same correction algorithm applied to the GPCTD.

O_2 time-series acquired with the different sensors used underwent large discontinuities, which were ubiquitously related to instrumental deficiencies. To face with this issue, the time-series was split into discrete segments according to the different sensors operated, all based on OceanGliders SOP (Lopez-Garcia *et al.*, 2022). The assembled proposed adjustments (gain) were applied to make the entire glider time-series continuous. Gain values applied for each discontinuity can be found in Appendix B table B1. Illustrative examples of profile corrections are presented in Appendix C Fig. C1. Sensors unit, range, precision and resolution can be found in Appendix D table D1.

2.2.2 CO_2 data

The response time of membrane-based sensors is a major constraint for profiling platforms (Fiedler *et al.*, 2013). Although the glider is a rather slow profiling device, with an average vertical speed of about $15cm/s$, the MINICO2 response time cause an appreciable hysteresis in vertical CO_2 profiles. A time-lag correction algorithm (Miloshevich *et al.*, 2004) has been applied on carefully smoothed vertical profiles of CO_2 (to minimize noise amplification caused by the processing algorithm), using the

following model, sequentially:

$$CO_{2,corr}(t) = \frac{CO_{2,raw}(t) - CO_{2,raw}(t-1)e^{\frac{-\Delta t}{\tau}}}{1 - e^{\frac{-\Delta t}{\tau}}} \quad (1)$$

Where $CO_{2,raw}(t)$ is the measured value at the time t, $CO_{2,raw}(t-1)$ is the measured value at the previous time stamp, Δt is the time between two measurements (1 second for raw measurements or 30 s for sub-sampled measurements), $CO_{2,corr}(t)$ is the time-lag corrected (TLC) measurement at t and τ is the response time. Previous studies have shown pronounced changes in τ that linearly depends on water TEMP (Fietzek *et al.*, 2014): the warmer the water, the faster the response time. In the absence of published values for the MINICO2 sensor, the linear relationship was determined empirically minimizing the difference in CO_2 between upcast and downcast profiles of a dive. Finally, raw CO_2 data recorded in ppm were converted in $\mu mol/l$ from manufacturer calculation sheet and using in-situ temperature and salinity values measured by the CTD.

2.2.3 CH_4 data

The measurement of CH_4 might be impacted by various external factors such as temperature, in-situ CH_4 or the moving speed of the glider. Main consequences are an artificially increasing CH_4 with decreasing temperature, an hysteresis between the upcast and the downcast phases of a profile and thermal and temporal lags (Meurer *et al.*, 2021, Russell-Cargil *et al.*, 2018). In the present study, these issues were first addressed by adapting the sampling strategy. Indeed, the glider was programmed to dive in deep multiple yos to limit the impact of varying environmental conditions. This way, it is expected that temporal changes in CH_4 (e.g. induced by natural seepage) would be more easily detectable compared to a situation where the glider would cross regularly strong temperature gradients. Comparison of CH_4 profiles between upcast and downcast phases enabled the computation of a lag in the sensor response time (τ) of about 6 minutes. The estimated sensor response time implies that CH_4 measurements are subject to a significant temporal smoothing, particularly during phases of rapid vertical variation such as near inflection points in the profiles. Adjusted CH_4 ($CH_{4,corr}$) were thus calculated following the Meurer *et al.*, 2021 algorithm:

$$CH_{4,corr}(t) = CH_4(t+\tau) \quad (2)$$

where t is the time, while τ varies according to the sensor used (Appendix A table A1). Sensors unit, range, precision and resolution can be found in Appendix D table D1.

2.2.4 ADCP data

For the purpose of this project, the ADCP was programmed to obtain current profiles with a high-resolution. Values of main tunable parameters can be found in Table 1. The method used to retrieve ocean currents is the "shear method" (Visbeck, 2002) to subtract the unknown motion of the glider from the absolute water velocity calculated by the ADCP.

Table 1. ADCP configuration and processing

Parameter	Description	Values
Position	Sensor mounting	Downward looking
NPING	Number of ping averaged	4
CS	Cell size	2 m
CN	Number of cells	15
SR	Sampling rate	10s

It is worth noting that glider ADCP measurements must undergo several quality control steps before profiles of ocean velocity can be properly estimated. It is a critical issue and this must be done with great caution. Pasqueron de Formmervault *et al.*, 2018 developed a number of tests specifically adapted for the SeaExplorer glider. As stated in Pasqueron de Fommervault *et al.*, 2018, ocean velocity data retrieved from glider-mounted ADCP show a mean difference of 1.5 cm/s compared to reference mooring data. This value corresponds to a simple yo pattern using a SeaExplorer glider. In our case, using repeated multi-yo patterns until August 2023, followed by spiral multi-yos from August 2023 to April 2024, the uncertainty is likely higher than 1.5 cm/s. Based on our preliminary assessments, it may remain below 10 cm/s, although this upper bound should be considered with caution.

The quality of the data set was assessed at the end of each mission by comparing the depth-integrated current between two consecutive surfacings to the mean current deduced from the hydrodynamical model of the glider (model calculating the glider's position according to the various navigation parameters recorded during its yo).

The processing of current data with the "shear method" requires reconstructing vertical profiles by cutting the time-series on the basis of dives. In case of multi-yos, which are not optimal to retrieve best quality current measurements, all yos between two consecutive surfacings are merged to reconstruct a single average current profile. Since the tidal current oscillates over a period of about 12 hours, its oscillations are therefore almost always averaged over the duration of a 10-hours dive. To process the ADCP data, overlapping shear values were averaged over a given interval of 2 m to determine a mean shear profile for a dive.

While ADCPs are primarily used to measure the velocity of the particles, they can also provide information about the backscatter index (BI) that in turn is a proxy of the density of scatterers in the water. This information is measured in the form of the intensity of the received reflections, also referred to as the backscattering strength or signal amplitude. The method to retrieve BI from raw ADCP measurments employs a formula based on the sonar equation for sound scattering from small particles (Deines, 1999; Van Haren and Gostiaux, 2010; Mullison, 2017; Gentil *et al.*, 2020):

$$BI = EI + Tl_g + Tl_w \tag{3}$$

EI is the echo intensity estimated from ADCP signal amplitude from all beams using the Mulison (2017) equation. Tl_g is the beam spherical spreading, which is simply a geometric term due to the cone shape of the acoustic beams. Tl_w is the

transmission loss by the sound absorption in seawater calculated according to Francois and Garrison (1982) and taking into account absorption by boric acid and magnesium sulfate.

Finally, glider ADCP measurements also directly allows to compute vertical velocities by subtracting the glider motion from pressure measurements:

$$U_{z_G}(z,t) = \frac{\Delta z(z,t)}{\Delta t(z,t)} \tag{4}$$

where $\frac{\Delta z(z,t)}{\Delta t(z,t)}$ is the temporal derivative of the glider depth between two consecutive ADCP measurements. This computation is not accurate enough to obtain vertical oceanic velocities (O(1 mm/s)) but adequate to measure large vertical movements of scatterers such as CO_2 droplets (O(1 cm/s)).

2.3 Quality control process

Based on UNESCO's best oceanographic practices (https://repository.oceanbestpractices.org/handle/11329/413), which are also used for Argo floats, an objective and automatic quality control (QC) process was applied. Quality flags (QF) are composed of four quality values (Table 2).

The procedure allows to flag outliers but may be deficient in identifying some erroneous data. Tests presented hereafter relate

Table 2. Quality flag scheme

Quality flag value	Quality flag name	Definition
1	Good	Passed quality control
2	Not evaluated	QC test not performed
3	Suspect	Failed subjective QC test
4	Bad	Failed objective QC test
5	Below detection level	Applicable for CH_4 data below the sensor detection level (3 $nmol/l$)

to the other variables and are based on published methods (Pouliquen 2011, Schmechtig *et al.*, 2016) and recommended by the scientific community within international programs, such as EGO quality control manual for CTD and BGC (BioGeoChemical) data (https://archimer.ifremer.fr/doc/00403/51485/92689.pdf, 2022).

A gross filter is applied on observed data using a global range test first (Table 3) with min and max values taken from World Ocean Atlas 2018 documentation (Garcia *et al.*, 2019).

Values that fail this test are flagged with a QF = 4. To our knowledge there are not yet international recommendation for CH_4 and CO_2, thus values were chosen based on *in situ* measurements from MAYOBS cruises.

For all parameters, data acquired when the CTD pressure is negative (i.e. in-air measurement) were flagged bad (QF = 4).

Furthermore, a large difference between sequential measurements, where one measurement greatly differs from adjacent ones, were also flagged bad if failing the following algorithm (only used to identify spikes in temperature, salinity and O_2 profiles, EGO quality control manual, 2022):

Table 3. Global range test derived from World Ocean Atlas 2018 climatology used for QC

Parameter	Min value	Max value
Temperature [°C]	4	30
Salinity [PSU]	34.7	35.3
Dissolved oxygen [$\mu mol/kg$]	100	220
Dissolved CH_4 [$nmol/l$]	0	2000
CO_2 [$\mu mol/l$]	5	100

$$Test = |\frac{V2-(V3+V1)}{2}| - |\frac{V3-V1}{2}| \quad (5)$$

where V2 is the measurement being tested as a spike, and V1 and V3 are the values preceding and ensuing. The V2 value is flagged when the test value exceeds:

TEMP : 6.0°C for PRES < 500 db or 2.0°C for PRES $\geq$ 500 db

SAL : 0.9 for PRES < 500 db or 0.3 for PRES $\geq$ 500 db

O_2 : 50 $\mu mol/kg$ for PRES <500 db or 25 $\mu mol/kg$ for PRES $\geq$500 db

To our knowledge there are to date no international recommendations for CH_4 and CO_2 yet. Thus, no spike test was applied on these variables.

Finally, subjective visual inspection was performed for each variable to identify outliers that were not flagged by the automatic and objective procedure. These measurements were associated with a QF = 3.

Membrane-based sensors (CO_2 and CH_4) are also deficient at high glider's speed (lag cannot be compensated correctly). Thus, CO_2 and CH_4 data acquired at glider's speed exceeding 0.25 m/s were flagged and excluded. This usually occurred when the glider rarely ascended in an alarm state.

All data provided has been quality controlled. Therefore, QF = 2 is not used in this data set.

Following these various objective and subjective tests, the remaining data volume of each data is provided in Appendix E table E1.

Every 6 months, a reassessment of the processing chain (algorithm, QC) and delayed mode adjustments (drift, offset) is proposed.

3 Results and discussion

3.1 Hydrological data set

Hydrological data presented are adjusted and associated with a QF = 1.

Time-series of temperature, salinity and potential density are presented in Fig. 3, averaged vertical profiles are presented in

Fig. 4 and temperature-salinity diagram exhibiting the different water masses is shown in Fig. 5.

As for temperature, vertical profiles exhibit a relatively warm upper layer ($\sim$ 0-100 m, 26-30 °C). The seasonal thermocline (steep thermal gradient of $\sim$ 0.1 °C/m) is observed between $\sim$ 100-200 m and the permanent thermocline is located at $\sim$ 500 m and is mainly composed of South Indian Central Water (SICW, Miramontes *et al.*, 2019). Below 500 m, temperature are in the range 5-10 °C, with a minimum reached below 1,000 m. In this layer, both Red Sea Water (RSW), that enters into the Mozambique Channel from the north, and Antarctic Intermediate Water (AAIW), that enters from the south are found (Miramontes *et al.*, 2019).

The vertical distribution of the salinity is more complex. Overall, the upper layer is characterized by values ranging from $\sim$ 34.7 and 35.5 PSU. A subsurface salinity maximum is observed at $\sim$ 200-300 m with salinity values reaching up to 35.5 PSU. At around 600 m, a local salinity minimum (34.6-34.8 PSU) is observed but followed by a slight increase to reach $\sim$ 34.85 below 1,000 m.

Deeper in the water-column (i.e., below $\sim$ 100 m), the variability in hydrological properties is lower. However, disruptions in the vertical distribution of temperature and salinity is visible, such as between June and July 2022 (between the gray dotted lines in Fig. 3) and can be attributed to the general circulation of the area or the mesoscale variability. Below 1,000 m the variations are $\sim$ 1°C and $\sim$ 0.1 for temperature and salinity respectively (Fig. 6).

Most of the temporal variability is observed in the surface layer, above the 1024 kg m^{-3} isopycnal. These changes are particularly obvious in the temperature-salinity diagram (Fig. 5) indicating the succession of two distinct water-masses (Collins *et al.*, 2016). Indeed, low salinity are typical of the Tropical Surface Water and contrasts with the higher salinity Subtropical Surface Waters (Di Marco *et al.*, 2002). Surface temperature exceeding 29°C (which are regularly observed from December to April, Fig. 4 and 7) can also be the signature of the influence on the South Equatorial Current that contains Pacific waters (Di Marco *et al.*, 2002) or associated to the transient presence of mesoscale eddies. Finally, and according to Wyrtki (1971), seasonal processes (and episodically tropical storms) may also account for the observed variability. Highest sea-surface temperatures and low salinity are generally observed during austral summer while in winter, colder and saltier waters dominate. This seasonal variability is observed in this part of the water column (Fig. 7), with warm ($\sim$ 27 – 28 °C) and salty ($\sim$ 35.3 – 35.4) surface waters from November 2021 to July 2022 and from October 2022 to July 2023 during warm and humid austral summer in Mayotte.

The analysis of the data set also highlighted the importance of smaller temporal scales processes. In particular, vertical fluctuations of potential density levels (and temperature and salinity) increasing as it gets close to the bottom were observed at a $\sim$ 12 h period (Fig. 7). Likely a result of internal tides, the sampling strategy chosen consisting of deep multi-yos unfortunately does not allow their quantification (section 2.2.4).

3.2 Dissolved gas data set

Similarly to the hydrological data set, data presented are adjusted and associated with a QF = 1.

Measured O_2, CO_2 and CH_4 concentrations by the glider are shown in Fig. 3. Typical vertical distributions are observed (Fig. 4) and can be explained by ubiquitous physical (e.g., dissolution, sea-air exchanges) and biological oceanic processes

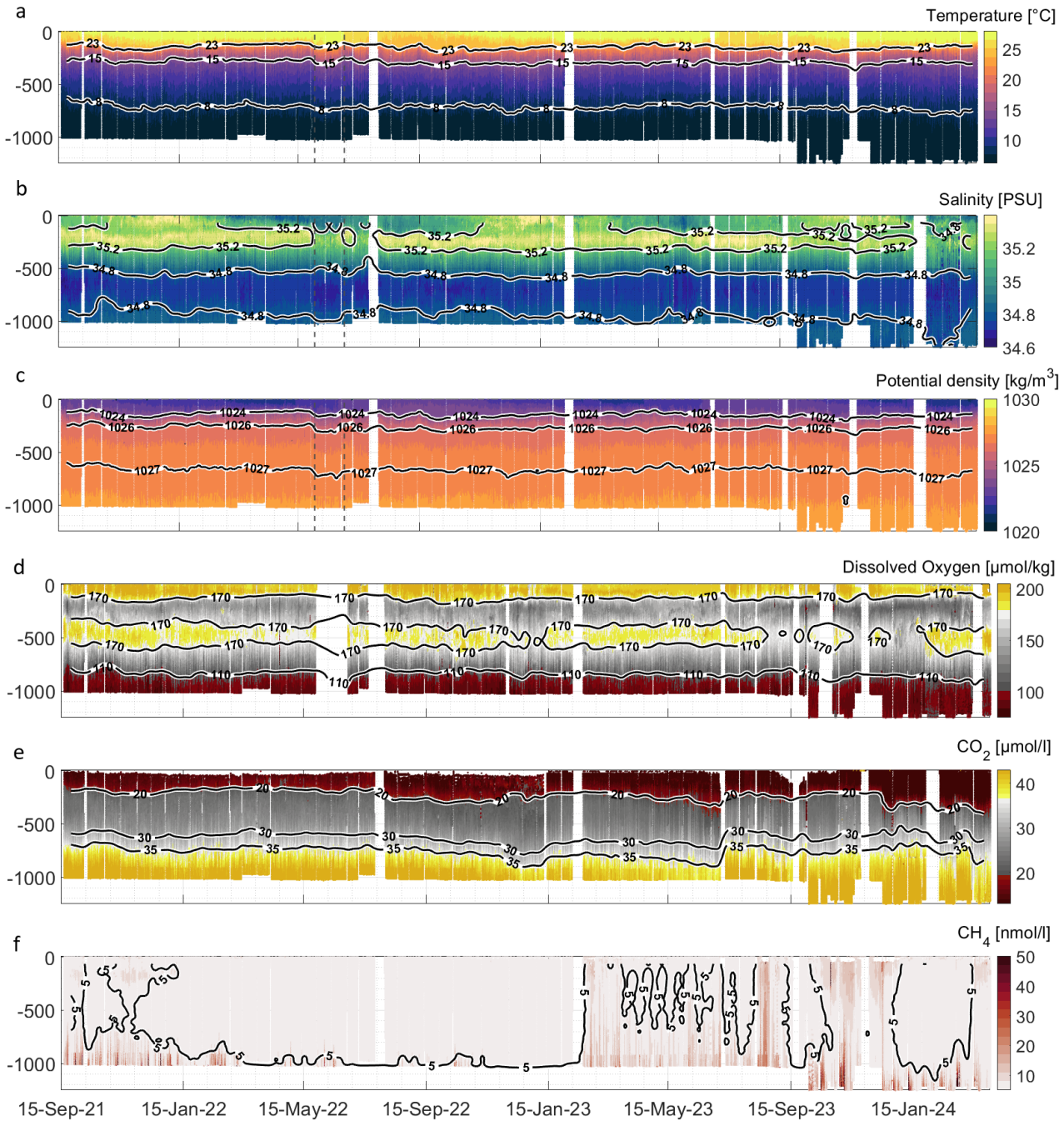

Figure 3. Temperature (a), salinity (b), potential density with reference pressure of 0 dbar (c), dissolved oxygen (d), CO_2 (e) and CH_4 (f) Hovmöller diagram in function of depth (Y-axis) and time (X-axis). Isolines are calculated by applying a Gaussian filter of size 7 to each data field. White areas correspond to time periods with no data due to sensor downtime or glider recovery.

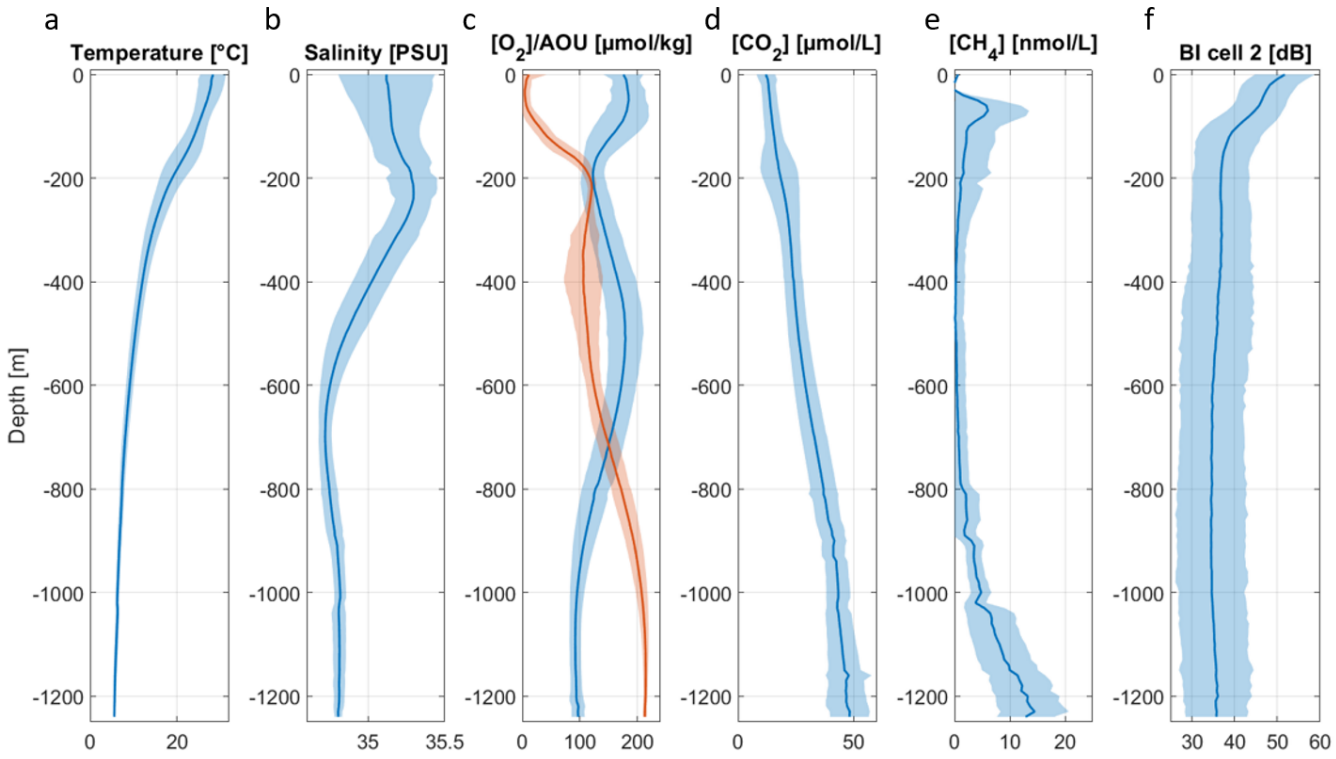

Figure 4. Averaged vertical profiles of temperature (a), salinity (b), O_2 (blue) and apparent oxygen utilization (AOU, orange) (c), CO_2 (d), CH_4 (e) and backscatter index (BI) calculated from the cell 2 of the ADCP (f) over 10 meter bins for the whole data set with variability represented as ± 2 standard deviations (shaded areas).

(photosynthesis and respiration).

High O_2 concentrations corresponding to oxygen saturation concentration are measured (O_2 concentrations of about 180-200 $\mu mol/kg$, apparent oxygen utilization between 0-20 $\mu mol/kg$, Fig. 3 and 4) at the surface layer (0 - 100 m) because of both dissolution from the atmosphere and O_2 production by phytoplankton. The study area, located off the coast of Mayotte, is generally characterized by oligotrophic conditions, typical of tropical oceanic regions (Ternon *et al.*, 2014). Such conditions are associated with low concentrations of nutrients in surface waters, which constrain primary production and consequently limit biological oxygen supersaturation. Nevertheless, the presence of detectable surface O_2 saturation suggests that, despite low nutrient availability, the prevailing light conditions and water column stratification support moderate phytoplankton activity in the upper layer. As the distance to the surface increases O_2 generally declines, due to O_2 removal by consumption of deep-water organisms and by the decomposition of organic material by bacteria (Hedgpeth, 1957). In the glider data set, minimum O_2 values (O_2 in the range 70-100 $\mu mol/kg$) are observed below 1,000 m. In spite of this decrease, O_2 content rise to a subsurface maximum at $\sim$ 400-500 m with values reaching up to 200 $\mu mol/kg$. This high O_2 core (> 180 $\mu mol/kg$) is characteristic of the South Indian Central Water (Di Marco *et al.*, 2002).

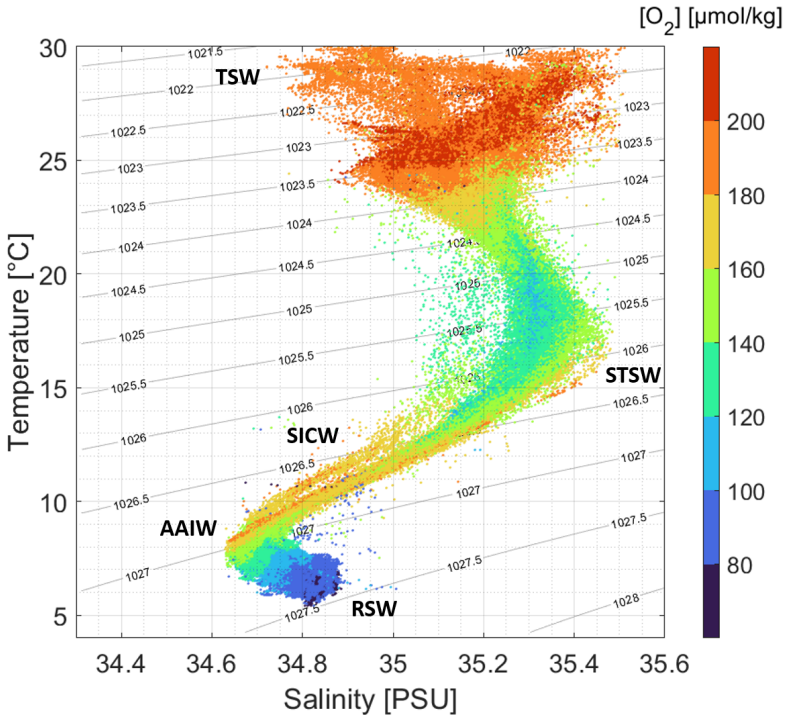

Figure 5. Temperature salinity diagram. The color indicates the O_2 concentration and the water masses associated are annotated. TSW stand for Tropical Surface Water, STSW for Subtropical Surface Waters, SICW for South Indian Central Water, AAIW for Antarctic Intermediate Water and RSW for Red Sea Water.

Regarding the CO_2 vertical distribution (Fig. 4), it is essentially the reverse of O_2, mainly because both gases are involved in the same biological processes in opposite ways. In the surface, photosynthesis consumes CO_2 and thus concentrations are low ($\sim$ 15 $\mu mol/l$). In deeper waters, CO_2 concentration increases as respiration exceeds photosynthesis and decomposition of organic matter adds additional CO_2 to the water. In this data set, minimum CO_2 concentrations are found in the surface layer (0 - 100 m) with concentrations measured between 15-20 $\mu mol/l$, and maximum CO_2 values are measured below 1,000 m depth with concentrations generally higher than 40 $\mu mol/l$ and sporadically exceeding 50 $\mu mol/l$. Moreover, the signature of SICW with its oxygen maximum at $\sim$ 400-500 m (Di Marco *et al.*, 2002) is not matched by a CO_2 minimum at this depth.

The vertical distribution of CH_4 differs significantly from the ones of O_2 and CO_2 (Fig. 3 and 4). Almost no CH_4 is detected in the layer 0-600 m (values are below 10 $nmol/l$). This is not surprising because the ocean is supposed to be depleted in CH_4 apart from specific areas (methanogenesis in marine sediments, natural seepage by volcanoes or hydrothermal vents, pollution, Oremland *et al.*, 1978). Most of CH_4 increases occur in the 900-1,250 m layer where the sampling effort is maximum. In this layer, when CH_4 anomalies are detected (above the sensor detection limit), a gradient of increasing concentration with depth is observed. High values relative to the background are regularly observed with a maximum recorded on February 18, 2022, when CH_4 reached 120 $nmol/l$ at a 1,000 m. Although observations above 900 m are scarcer than below, several vertical

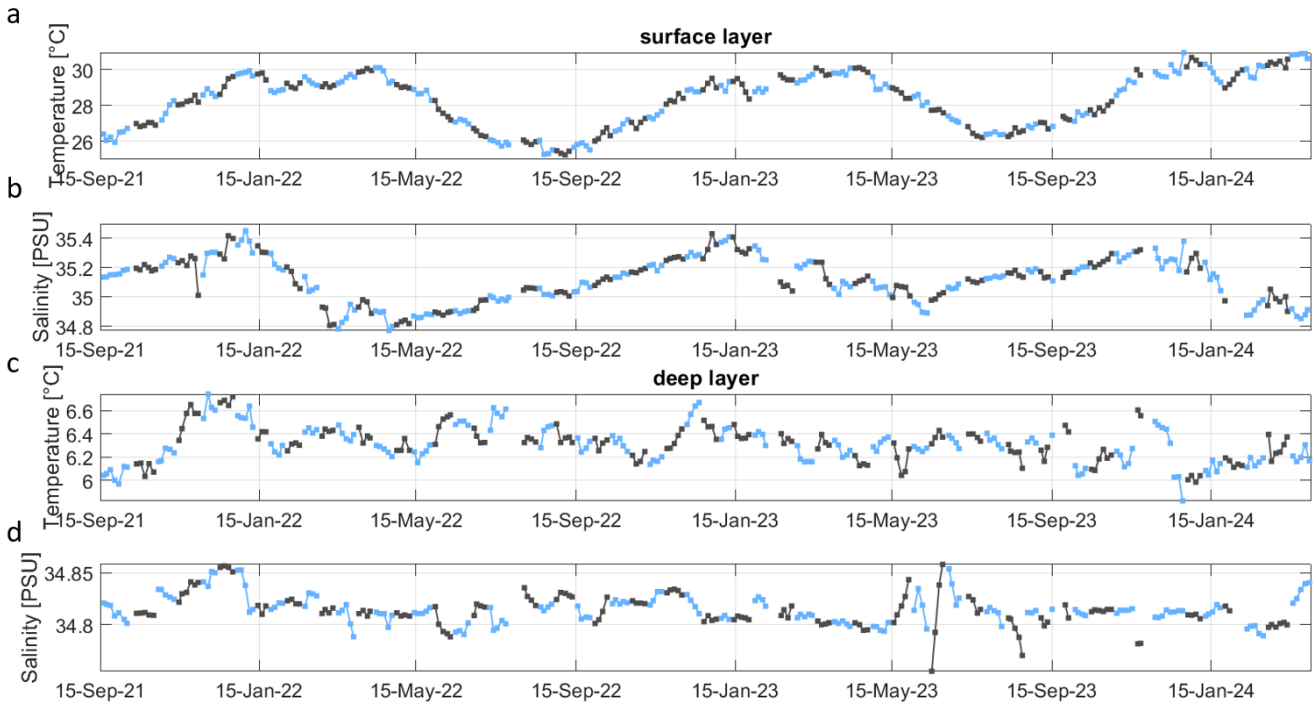

Figure 6. Surface layer (0 to 5 m) daily average temperature (a) and salinity (b) and deep layer (950 to 1,250 m) daily average temperature (c) and salinity (d). Color alternation reflects the succession of glider missions.

profiles also show significant CH_4 concentrations up to 700 m.

There is also variability in dissolved gas concentrations, with periods (e.g., September 2022 to mid-October 2022 and mid-November 2022 to February 2023) of decreasing CH_4 or CO_2 concentrations not yet explained (Fig. 8).

Considering the amount of data produced, semi-automatic methods are thus required to reduce this data set to relevant information. Here we focus on parameters that track magmatic fluid emissions (CO_2 and CH_4) and define anomalies as observations that deviate significantly from the majority of the data.

Identifying anomalies (that refer to fluid emissions) is challenging since it requires the decoupling between natural variability (e.g., water masses, seasonality) and changes induced by fluid emissions. In particular, CO_2 and CH_4 signals are characterised by slowly varying background values related to dissolved gases accumulation and flushing over a large area. The CH_4 baseline is low (<10 $nmol/l$) and has a magnitude of variability of about 6 $nmol/l$. On the other hand, CO_2 baseline is more elevated ($\sim$ 45 $\mu mol/l$ at a 1,250 m), because of the natural presence of CO_2 in seawater and CO_2 anomalies below 900 m, but fluctuations around the mean values do not exceed $\sim$ 3 $\mu mol/l$.

Results also show that both CO_2 and CH_4 baselines have similar temporal evolutions, supporting the hypothesis that this variability is likely to be real. For the purpose of anomaly detection, the baseline was thus subtracted to the raw data:

$$Gas, anomaly_{deep}(t) = Gas, measured_{deep}(t) - Gas, baseline_{deep}(t) \quad (6)$$

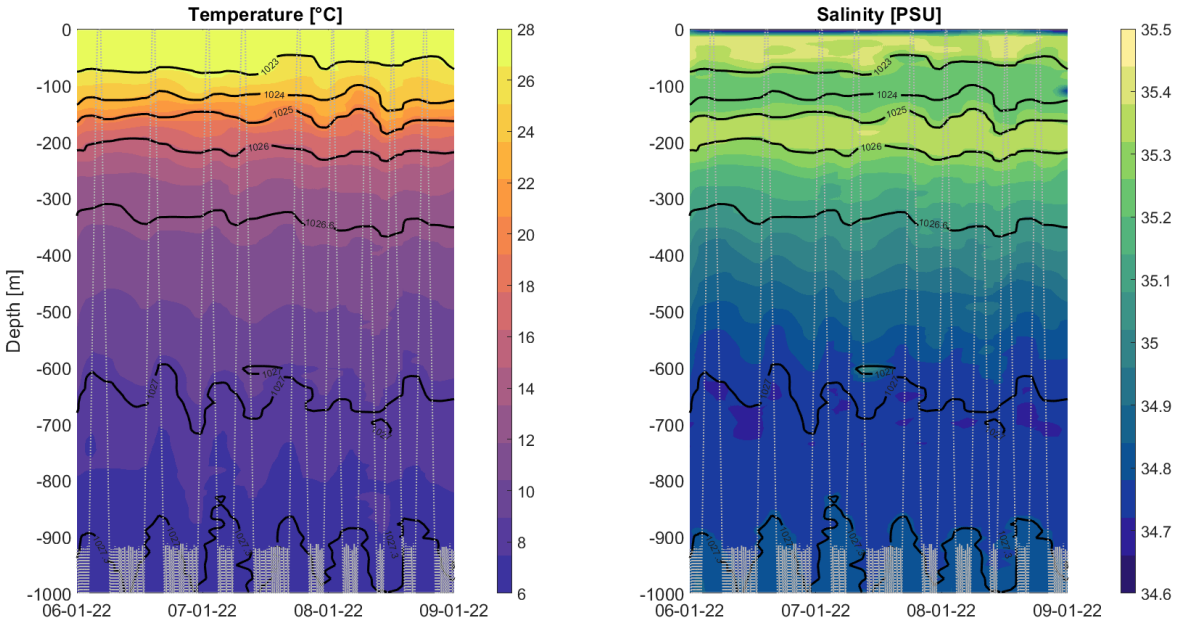

Figure 7. High-frequency ($\sim$ 12 h period) oscillations of temperature (a) and salinity (b) in function of depth (Y-axis) and time (X-axis). Glider depth is represented by the light gray dotted-line and isopycnals are also calculated and displayed in black. Data are interpolated with a triangulation-based cubic interpolation over a 12 m grid.

However, the cause of this low-frequency variability still remains to be clarified. At this time, it is not clear if baseline fluctuations are related to accumulation/dispersion processes or induced by changes in fluid emissions rate, both compatible with the chosen anomaly definition.

Of the 22000 profiles, 5 % were associated with significant CH_4 anomalies (greater than the sensor detection limit plus twice the standard deviation) and 2 % with significant CO_2 anomalies related to dissolved gas emissions (same definition as for the CH_4).

Data show that CO_2 and O_2 have similar patterns. Such a co-variation is expected in the ocean and related to biotic processes. Examining this relation at depth > 700 m (i.e., below the STSW) indeed confirms a high CO_2 and O_2 correlation (linear correlation coefficient, $R^2 = 0.96$). Several single measuring points deviate from the linear relationship (Fig. 8). They are all found in the upper curve, i.e. at depth where CO_2 is high and O_2 low. Most of these points are also associated independently with high CH_4 concentrations, which strongly suggests that these CO_2 anomalies are related to a non-biotic CO_2 source.

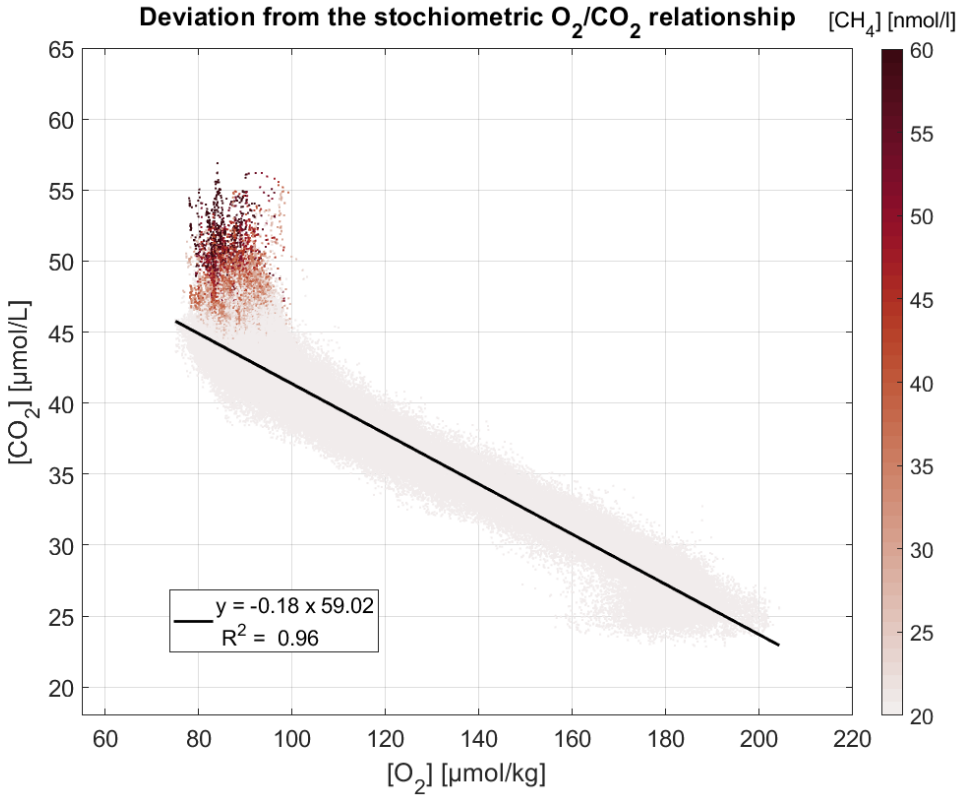

Figure 8. O_2/CO_2 relationship below 700 m, the colorbar indicates the CH_4 concentration. Data are taken from September 2021 to January 2023 and below 600 m.

3.3 Ocean current and acoustic backscatter data set

ADCP-derived water currents show a large profile-to-profile variability that encompass, in all likelihood, spatial and temporal variability. Strongest currents are measured in the surface (0-100 m layer) but velocities remain elevated down to 1,250 m (Fig. 9).

Overall, eastward velocities do not exhibit clear patterns. Values are oscillating with no preferential direction (Fig. 9). Conversely, northward velocities are characterized by a distinguishable temporal variability. From several weeks to several months, the current direction changes, with long periods of time when the direction of flow remains unchanged. The strongest currents appear to be aligned with the continental slope (north-south axis), which may be related to barotropic currents.

Strong deep currents ($\approx$ 0.4 - 0.5 m/s) below 900 m are also present in the area, locally highly variable with strong interactions with the bathymetry and the tide (Fig. 9).

Backscatter data estimated from ADCP measurements and expressed as the backscatter index (BI) are represented on Fig. 4 as an averaged profile. This averaged profile primarily depicts water-masses optical properties changes which are determined

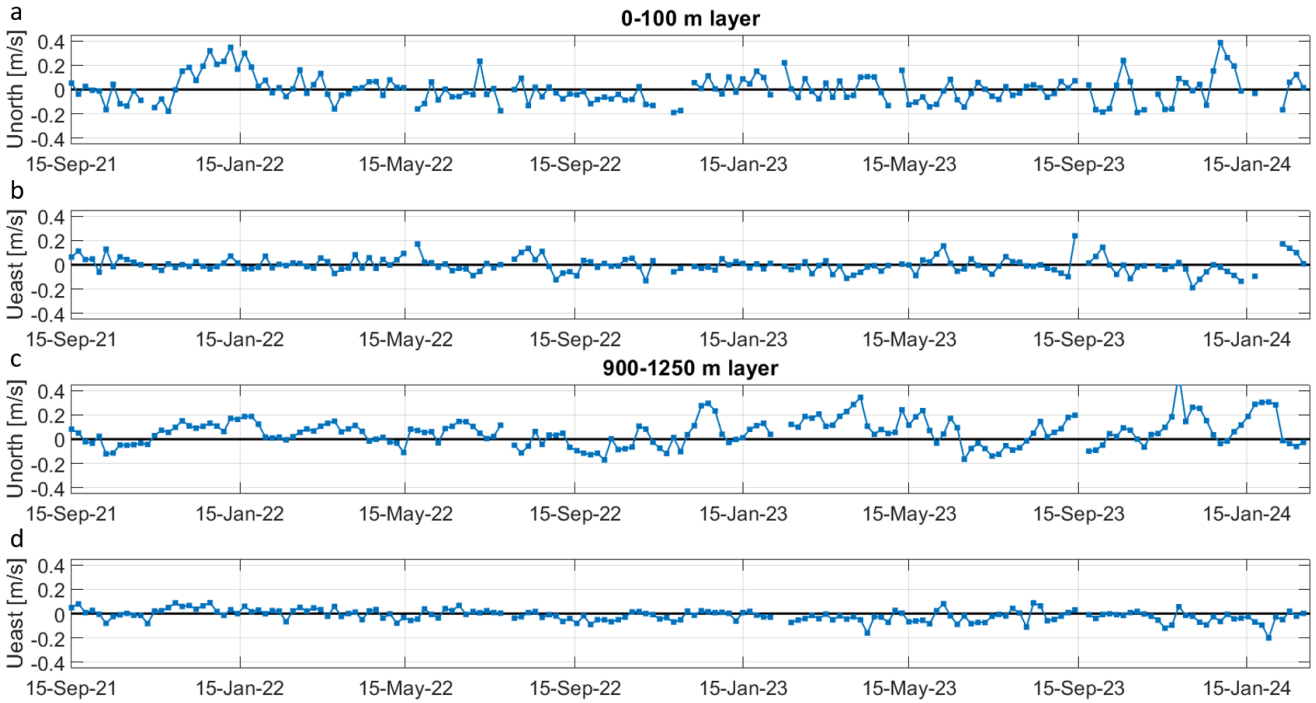

Figure 9. Time-series of northward (a) and eastward (b) velocities measured by the ADCP in the 0-100 m layer and time-series of northward (c) and eastward (d) velocities measured by the ADCP in the 900-1,250 m layer. The data shown correspond to daily mean values, computed separately for the depth layers: the surface layer (0–100 m) and the deep layer (900–1250 m).

by phyto- and zoo-plankton abundance, mineral particles concentration (Mullison, 2017; Gentil *et al.*, 2020). Thus, and as it can be expected, BI shows maximum values in the surface layer (0-100 m), where most of the biological activity takes place. Deeper in the water-column, BI is generally lower, although sometime peaking at the level of the South Indian Central Water and in the $\sim$ 900-1,250 m layer when crossing dissolved gases plumes or moving around the seafloor.

Similarly, the BI variability in the surface mirrors changes in temperature and salinity to a certain extent and several glider dives showed a BI increase at depth, when the glider approaches the continental shelf. This variability is not fully understood and likely to be a multi factor cause resulting from a decoupling of the surface, subsurface and deep dynamics. Whatever the processes envisioned, in all likelihood, a direct contribution of magmatic fluid emissions can be discarded.

In the other hand, BI profiles are noisy and variable with depth and despite this large variability, the signature of bubble/droplets appears to be unambiguous, associated with a large density of positive spikes of great amplitude and associated vertical velocity anomalies of about 15 cm/s, which is the ascent velocity of millimeter-sized gas droplets in seawater (Rehder *et al.*, 2009; Leblond *et al.*, 2014, Fig. 10). BI increases in the deep layer were considered to be related to bubble/droplet plumes if several consecutive BI values exceed $\sim$ 50 dB in at least 6 cells of the ADCP to discard the few possible misdetection at this depth. This was used as a criterion for BI anomaly detection but each dive was also visually inspected.

Of the 22,000 profiles, 457 ($\sim 2\ \%$) were associated with significant BI anomalies. The relative low occurrence of BI detections indicates that bubble/droplet plumes are likely to be of limited spatial extension ($\sim$ hundreds of meters) especially compared with dissolved and neutrally buoyant gas plumes.

Although associating BI detections directly to a fluid emission active site is complex (uncertainty in glider positioning, tilt of droplets/bubbles plumes of several hundred meters because of deep and tidal currents), data show that most of known active sites were indeed identified by the glider. 95% of BI detections are found within a radius of 700 m from an active site and the remaining 5% always at a distance less than 1.6 km.

Repeated dissolved gases and BI anomalies in the 800-1,250 m layer (Fig. 10) provide evidence that elevated CO_2 anomalies in the 900-1,250 m layer are related to magmatic fluids emissions from the seafloor.

BI detections outside of the 95th percentile are observed around the Horseshoe zone may arise from intermittent, small, unidentified sites or false detections. Further analysis is needed to confirm the nature of these detections.

Temporal variations in dissolved gas concentrations (CH_4 and CO_2) and BI anomalies are presumably caused by a complex array of factors, including spatial variability related to the glider pathway. However, on the basis of our current knowledge, we assume that a large part of the observed changes can indeed be related to the variability of seafloor fluid emissions in the Horseshoe area as well as the orientation and direction of the current at depth.

3.4 Discussion

Over the 30 months of deployments, values of CH_4 and CO_2 show some interesting patterns, with a large profile-to-profile variability observed in dissolved gas deep anomalies. High anomaly values exceeding the detection limit of the sensor plus two times the standard deviation (20 $nmol/l$ for the CH_4 and 7 $\mu mol/l$ for the CO_2 anomalies) are observed throughout the time-series. In the 900-1,000 m layer (more than 90% of the data set), the maximum CH_4 anomaly value is reached on February 21, 2022 (116.9 $nmol/l$) and the maximum CO_2 anomaly value on September 04, 2022 (29.2 $\mu mol/l$).

Although a direct correlation between currents and gas anomalies is speculative, our data suggests a potential impact of mesoscale structures on gas concentrations in the 900-1,250 m layer. The underlying processes are still poorly understood from the sole analysis of the glider data set, but several processes would be worth to investigate (e.g., trapping of gas bubbles in stratified layers, lateral dispersion by mesoscale flows, vertical diffusion of dissolved gases, or upwelling induced by topographic features or internal waves). Furthermore, additional bottom current data could potentially be useful for this analysis.

In order to assess the spatial distribution, anomalies are plotted on maps (Fig. 11). This provides a comprehensive view of the area impacted by fluid emissions, over the 30 months duration of deployments. On Fig. 11, data are binned in 7 discrete concentrations intervals and superimposed from weakest to strongest values with circles of decreasing size. Only data that exceed criteria of detection are colored, and the maxima of the colorbar are equal to the 99th percentile. Highest gas anomalies were all observed in the center and in the immediate vicinity of the Horseshoe edifice and the magnitude of the anomalies progressively decrease as the glider moves away from the center. The radius of gas anomalies detection is around 10 km, and the total area impacted by fluid emissions spread over about 300 km^2. These maps, that gather all data since September 17,

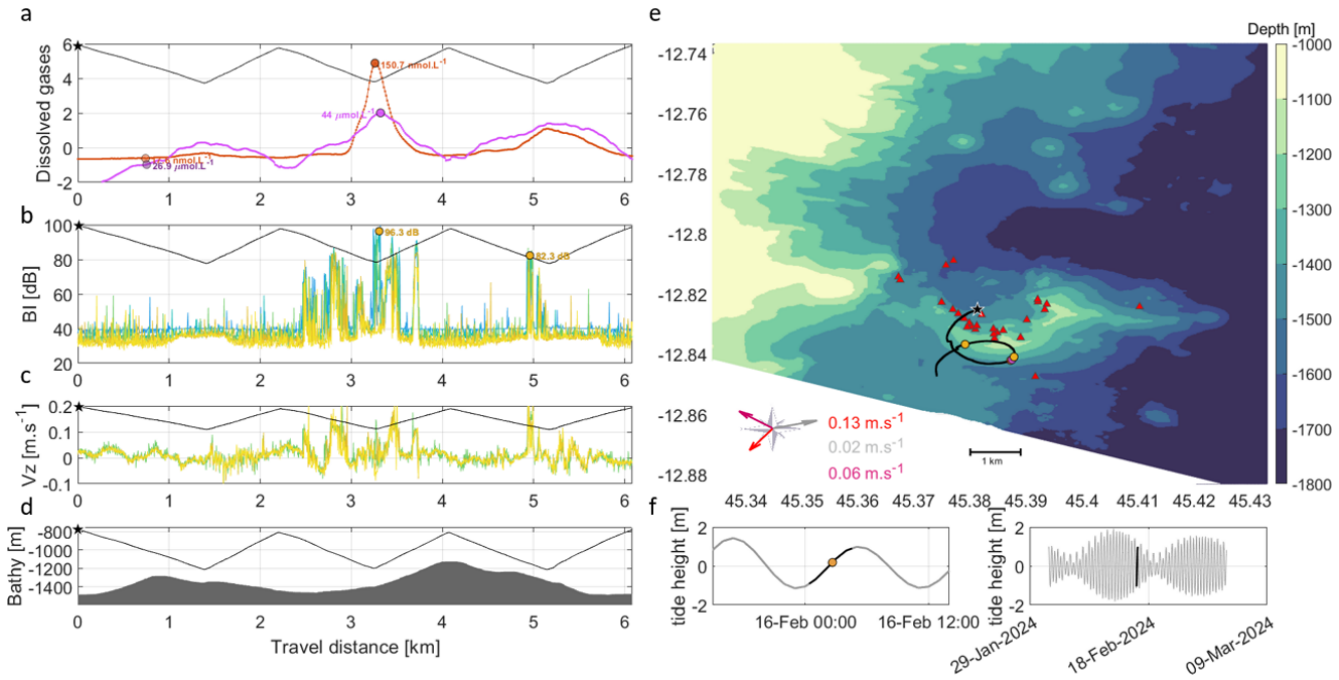

Figure 10. Example of a glider between 800-1,250 spiral track carried out above known fluid active sites. On the left side : CO_2 and CH_4 concentrations are represented respectively in red and purple centered and reduced (to get a common representation of the two dissolved gases despite the different baselines and anomalies) as a function of the dive progress (a). The minimum and maximum of each data are represented by a circle. BI data calculated from each paired cell of the ADCP (b), followed by vertical velocity calculated from the ADCP data (c) data and finally bathymetric profile along this dive (d). On the isobath map of the Horseshoe area with the underwater glider position in black including the plot of direction and velocity for different currents calculated during this dive (surface geostrophic current in red, ADCP-calculated 800-1250 m deep current in purple and tidal current in grey) (e) and the local tide height (f). Surface geostrophic current is estimated from sea level anomalies (SLA) data computed with respect to a twenty-year [1993, 2012] mean (https://doi.org/10.48670/moi-00149). Tidal current parameters are computed with MIKE21 model.

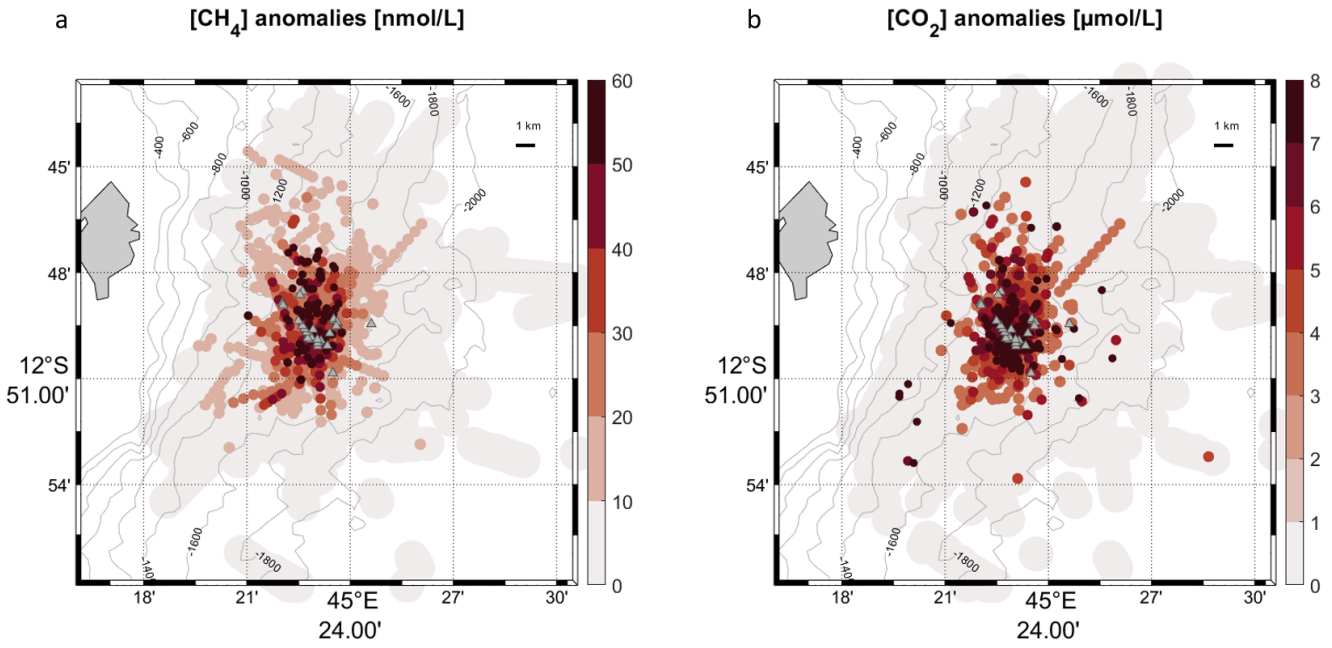

Figure 11. Map of CH_4 (a) and CO_2 (b) anomalies above the detection limit of these sensors recorded during the whole glider survey. The gray triangles are the active fluid emission sites identified with the multibeam echosounder during the REVOSIMA MAYOBS cruises (DOI 10.12770/070818f6-6520-49e4-bafd-9d4d0609bf7d) and validated by *in situ* visual observations with the ROV VICTOR during the GEOFLAMME cruise (DOI 10.17600/18001297).

2021, also show that the distributions of gases anomalies are not isotropic. In particular, relatively high concentration relative to the far field are observed northward which can highlight a preferred export direction for these quantities of dissolved gas.

Many questions still remain in our understanding of the underlying processes. We can for example mention the spatial decoupling between acoustic and dissolved gas plume or the contribution of physical factors in modulating the extension, direction and intensity of the plumes (currents, internal tides).

To face with these scientific challenges, the synergy between the glider with other observations and measurement tools (CTD cast, ROV, moorings), numerical models and satellite products is promising. Several studies in this direction have been initiated, and although clear results are not yet available, ongoing work is progressing steadily.

Reference data acquired during MAYOBS cruises allowed for a cross-calibration exercise of the dissolved gases sensors. An exercise has been carried out during MAYOBS25 cruise in September 2023 and MAYOBS30 cruise in September 2024 by harnessing two gliders on the CTD cast in order to compare dissolved gases from glider sensors and Niskin samples. The aim of these calibrations is to quantitatively calibrate dissolved gas sensors in order to calculate the fluxes of fluids emitted at the seabed. The database will be updated accordingly for the time period covered by this study once the CH_4 and CO_2 sensor

calibrations are finalized. Additional datasets will also be made available in the future, as the mission is ongoing. Since the project is funded by the French government, all validated data will be made publicly accessible.

4 Conclusions

The data set presented here demonstrates the feasibility of collecting long-term physico-chemical measurements (including CTD, ADCP and dissolved gases such as O_2, CH_4, and CO_2) using a glider platform over periods extending up to 30 months, with interruptions limited to deployment/recovery operations and brief maintenance interventions.

This is one of the few glider missions that has simultaneously sampled CH_4 and CO_2 data as well as the longest glider time series of these dissolved gas measurements that we are aware of. It also opens the possibility for new projects and research with the ability to detect and monitor CH_4 and CO_2 underwater distribution (e.g., GEORGE project (Next Generation Multi-platform Ocean Observing Technologies for Research Infrastructures, https://george-project.eu/), Hauri *et al.*, 2024).

The vertical distribution of hydrological, dissolved gas and BI data highlighted anomalies due to magmatic fluids in the Horseshoe area, while ADCP-calculated current depicted an active area subject to strong currents both at the surface and at depth.

The data analysis is still ongoing but the glider platform showed its ability to monitor, track and characterize seafloor fluid emissions mainly composed of CO_2 droplets off Mayotte Island. This experiment proves the feasibility of integrating a glider into a real-time early warning system. In particular, the continuous monitoring at a high spatio-temporal scale of the 0-1,250 m layer appears to be relevant to complement traditional oceanographic cruises (synoptic and high-quality data but with a limited temporal scale) and to ensure an operational observing system.

The robustness of the platform (SeaExplorer glider) has also been demonstrated thanks to this data set, with 901 days at sea over 929 days (97 % of its time spent at sea).

The quasi-permanence of elevated gas concentrations (CO_2 and CH_4) in the Horseshoe area support that fluid emissions are likely to have been continuous and detectable over the 30 months of the mission

Regular detections of acoustic plumes above all identified active sites have provided direct evidence of active seepage during the survey and the presence of bubble/droplets above 1,250m-depth.

Data availability. Raw and processed data are available from the SEANOE data center : https://doi.org/10.17882/99960 (Heumann *et al.*, 2024).

Appendix A

Table A1. Glider missions performed with deployment and recovery, glider used, mission ID and sensors serial numbers

Deployment	Recovery	Glider	Mission ID	ADCP	MINICO2	GPCTD	LEGATO	SBE43F	AROD	METS
17/09/2021	07/10/2021	SEA042	001	100584	39-636-18	0114		2610		1635
11/10/2021	27/10/2021	SEA042	002	100584	39-636-18	0114		2610		1635
29/10/2021	12/11/2021	SEA042	003	100584	39-636-18	0114		2610		1635
13/11/2021	29/11/2021	SEA042	004	100584	39-636-18	0114		2610		1635
30/11/2021	13/12/2021	SEA042	005	100584	39-636-18	0114		2610		1635
14/12/2021	27/12/2021	SEA042	006	100584	39-636-18	0114		2610		1635
28/12/2021	10/01/2022	SEA042	007	100584	39-636-18	0114		2610		1635
11/01/2021	21/01/2022	SEA042	008	100584	39-636-18	0114		2610		1635
22/01/2021	02/02/2022	SEA042	009	100584	39-636-18	0114		2610		1635
03/02/2022	16/02/2022	SEA042	010	100584	39-636-18	0114		2610		1635
17/02/2022	01/03/2022	SEA042	011	100584	39-636-18	0114		2610		1635
03/03/2022	14/03/2022	SEA042	012	100584	39-636-18	0408		3343		1635
15/03/2022	29/03/2022	SEA027	013	102759	39-636-18	0408		3343		1635
30/03/2022	10/04/2022	SEA027	014	102759	39-636-18	0408		3343		1635
13/04/2022	27/04/2022	SEA027	015	102759	39-636-18	0408		3343		1635
28/04/2022	12/05/2022	SEA027	016	102759	39-636-18	0408		3343		1635
13/05/2022	27/05/2022	SEA027	017	102759	39-636-18	0408		3343		1635
28/05/2022	11/06/2022	SEA027	018	102759	39-636-18	0408		3343		1635
12/06/2022	27/06/2022	SEA027	019	102759	39-636-18	0408		3343		1635
28/06/2022	08/07/2022	SEA027	020	102759	39-636-18	0408		3343		1635
10/07/2022	25/07/2022	SEA027	021	102759	39-636-18	0408		3343		1635
04/08/2022	16/08/2022	SEA017	022	102759	39-636-18	0408		3343		1635
17/08/2022	28/08/2022	SEA017	023	102759	39-636-18	0408		3343		1635
29/08/2022	12/09/2022	SEA017	024	102759	39-636-18	0408		3343		1635
13/09/2022	27/09/2022	SEA017	025	102759	39-636-18	0408		3343		1635
28/09/2022	11/10/2022	SEA017	026	102759	39-636-18	0408		3343		1635
12/10/2022	25/10/2022	SEA017	027	102759	39-636-18	0408		3343		1635
26/10/2022	08/11/2022	SEA017	028	102759	39-636-18	0408		3343		1635

Deployment	Recovery	Glider	Mission ID	ADCP	MINICO2	GPCTD	LEGATO	SBE43F	AROD	METS
09/11/2022	22/11/2022	SEA017	029	102759	39-636-18	0408		3343		1635
23/11/2022	06/12/2022	SEA017	030	102759	39-636-18	0408		3343		1635
07/12/2022	19/12/2022	SEA017	031	102759	39-636-18	0408		3343		1655
20/12/2022	02/01/2023	SEA017	032	102759	39-636-18	0408		3343		1635
03/01/2023	12/01/2023	SEA017	033	102759	39-636-18	0408		3343		1635
13/01/2023	28/01/2023	SEA027	034	102889	42-030-18		210554		59	1635
29/01/2023	08/02/2023	SEA027	035	102889	42-030-18		210554		59	2016
18/02/2023	02/03/2023	SEA017	036	102886	42-030-18		210554		59	2753
03/03/2023	16/03/2023	SEA017	037	102886	42-030-18		210554		59	2753
17/03/2023	30/03/2023	SEA017	038	102886	42-030-18		210554		59	2753
31/03/2023	14/04/2023	SEA017	039	102886	42-030-18		210554		59	2753
15/04/2023	29/04/2023	SEA017	040	102886	42-030-18		210554		59	2753
30/04/2023	14/05/2023	SEA017	041	102886	42-030-18		210554		59	2753
15/05/2023	29/05/2023	SEA017	042	102886	42-030-18		210554		59	2753
30/05/2023	12/06/2023	SEA017	043	102886	42-030-18		210554		59	2753
13/06/2023	26/06/2023	SEA017	044	102886	42-030-18		210554		59	2753
27/06/2023	10/07/2023	SEA017	045	102886	42-030-18		210554		59	2753
11/07/2023	24/07/2023	SEA023	046	103361	42-030-18	0284		2733		2753
28/07/2023	09/08/2023	SEA083	RD8	102880	43-186-18	0408		3489		2821
10/08/2023	24/08/2023	SEA083	RD9	102880	43-186-18	0408		3489		2821
25/08/2023	30/08/2023	SEA083	RD10	102880	43-186-18	0408		3489		2821
26/07/2023	09/08/2023	SEA023	047	103361	42-030-18	0284		2733		2753
12/08/2023	24/08/2023	SEA017	048	103361	42-030-18	0284		2733		2753
25/08/2023	04/09/2023	SEA017	049	103361	42-030-18	0284		2733		2753
30/08/2023	31/08/2023	SEA083	RD11	102280	39-636-18	0408		3489		2821
05/09/2023	12/09/2023	SEA017	050	103361	42-030-18	0284		2733		2753
13/09/2023	16/09/2023	SEA017	051	103361	42-030-18	0284		2733		2753
11/09/2023	16/09/2023	SEA083	RD12	101592	39-636-18	0408		3489		2821
23/09/2023	30/09/2023	SEA017	052	103361	42-030-18	0284		2733		2753
23/09/2023	30/09/2023	SEA083	RD13	101592	39-636-18	0408		3489		2821
02/10/2023	12/10/2023	SEA083	RD14	101592	39-636-18	0408		3489		2821
13/10/2023	01/11/2023	SEA083	RD15	101592	39-636-18	0408		3489		2821
02/11/2023	17/11/2023	SEA083	RD16	101592	39-636-18	0408		3489		2821

Deployment	Recovery	Glider	Mission ID	ADCP	MINICO2	GPCTD	LEGATO	SBE43F	AROD	METS
18/11/2023	28/11/2023	SEA023	053	102886	42-030-18		210554		59	2821
02/12/2023	15/12/2023	SEA017	054	103361	39-636-18	0284		2733		2821
29/11/2023	02/12/2023	SEA083	RD17	105522	39-636-18	0408		3489		2821
15/12/2023	23/12/2023	SEA083	055	102880	39-636-18	0408		3489		2821
15/12/2023	25/12/2023	SEA027	056	104651	42-030-18	0114		3343		2016
26/12/2023	09/01/2024	SEA027	057	104651	42-030-18	0114		3343		2016
10/01/2024	23/01/2024	SEA027	058	104651	42-030-18	0114		3343		2016
24/01/2024	09/02/2024	SEA027	059	104651	42-030-18	0114		3343		2016
10/02/2024	26/02/2024	SEA027	060	104651	42-030-18	0114		3343		2016
27/02/2024	14/03/2024	SEA027	061	104651	42-030-18	0114		3343		2016
16/03/2024	02/04/2024	SEA027	062	104651	42-030-18	0114		3343		2016

Appendix B

Table B1. Gain values applied to O_2 data depending on dive number with reference profiles acquired during MAYOBS cruises.

Profile	Gain
1-4547	1
4548-5349	1.21
5350-7022	1
7023-7796	1.37
7797-8197	1
8198-8389	1.24
8340-13058	1
13059-17884	0.81
17885-19042	1.33
19043-20025	1.22
20026-20240	1
20241-20352	1.10
20353-20635	1
20636-21138	1.36
21139-21450	0.76
21451-21913	1
21914-22047	1.32

Appendix C

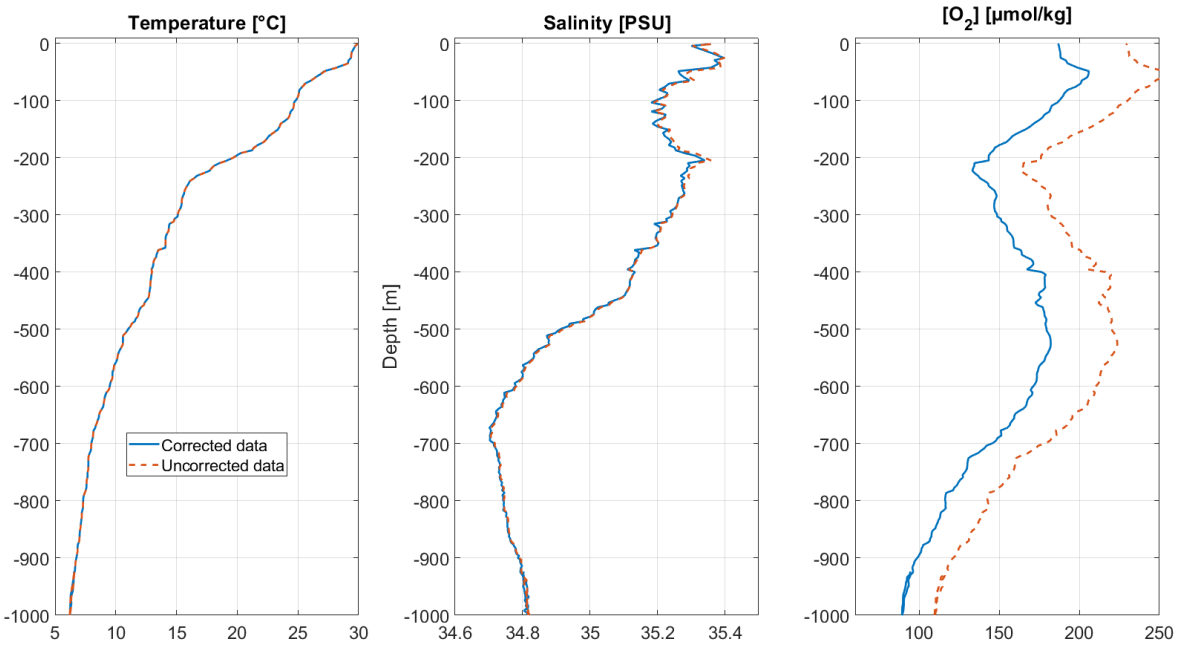

Figure C1. Vertical profiles of corrected (blue) and uncorrected (red) temperature, salinity, and O_2 concentration as a function of depth from dive 13089.

Appendix D

Table D1. Sensor informations

Parameter	Temperature		Conductivity		Dissolved oxygen		CO_2	CH_4	Ocean currents and BI
Manufacturer	RBR	Seabird	RBR	Seabird	JFE	Seabird	Pro Oceanus	Franatech	Nortek
Sensor	LEGATO	GPCTD	LEGATO	GPCTD	AROD-FT	SBE43F	Mini-CO_2	METS	ADCP
Unit	$°C$		mS/cm		$\mu mol/kg$		$\mu mol/l$	$nmol/l$	-
Range	-5 to +42	-5 to +42	0 to 85	0 to 90	0 to 425	0 to 120% of saturation	0 to 45000	10 to 1,000	post-processing
Precision	±0.002	±0.005	±0.003	±0.003	2% of measurement	2% of saturation	3% of measurement	50	post-processing
Resolution	< 0.00005	0.001	0.001	0.0001	0.01	0.5% of saturation	0.1% of measurement	5	post-processing
Sampling rate	1 Hz	1 Hz	1 Hz	1 Hz	1 Hz	1 Hz	1 Hz	1 Hz	0.1 Hz

Appendix E

Table E1. Percentage of total data going through QC (total number of points for each data is 2,232,706)

Quality flag value	Temperature	Conductivity	Dissolved oxygen	CO_2	CH_4
1 to 4	100%	100%	100%	100%	100%
1 to 3	95.9%	98.2%	99.3%	94.5%	97.1%
1	95.4%	92.4%	84.3%	78.9%	94.7%

Author contributions. All authors except GL took part in data acquisition of the data set by reviewing the data at two weeks interval since September 2021. HA was in charge of overall data processing and formatting, with the support of ML, PO and BL. All authors participated in the writing of the initial and revised versions of the paper; RE focusing more specifically on the dissolved gases data set, LP on the ocean current data set and SC on the acoustic backscatter data set.

Competing interests. The contact author has declared that none of the authors has any competing interests.

Acknowledgements. About data acquisition, we are grateful to REVOSIMA and to the financial support of the French ministries (Ministry of Overseas, Ministry of the Interior, Ministry of Higher Education, Research and Innovation, Ministry of Ecological Transition and Solidarity). We would also like to thank the French oceanographic fleet and the teams deployed on the RV *Marion Dufresne* during the MAYOBS cruises. We also thank the technical and piloting teams at Alseamar (Margaux Dufosse and everyone involved in this project) for making the data acquisition process as smooth as possible. Without whom nothing would have been possible in Mayotte, we thank the local community for allowing us to install a container on the Ballou quay. Last but not least, we would like to thank all those who made it possible for us to deploy, recover and repair the gliders in Mayotte, despite the hazards and often inconvenient timings (Caroline Bachet, Jules Heliou and Mayotteexplo).

References

Aiken C., Saurel J-M, Foix O. (2021). Earthquake location and detection modeling for a future seafloor observatory along Mayotte's volcanic ridge. Journal Of Volcanology And Geothermal Research, 418, 107322 (12p.). https://doi.org/10.1016/j.jvolgeores.2021.107322.

Collins, C., J. C. Hermes, and C. J. C. Reason (2016), First dedicated hydrographic survey of the Comoros Basin, J. Geophys. Res. Oceans, 121, 1291–1305, doi:10.1002/2015JC011418

Collins, C., J. C. Hermes, and C. J. C. Reason (2014), Mesoscale activity in the Comoros Basin from satellite altimetry and a high-resolution ocean circulation model, J. Geophys. Res. Oceans, 119, 4745–4760, doi:10.1002/2014JC010008.

K. L. Deines, "Backscatter estimation using Broadband acoustic Doppler current profilers," Proceedings of the IEEE Sixth Working Conference on Current Measurement (Cat. No.99CH36331), San Diego, CA, USA, 1999, pp. 249-253, 10.1109/CCM.1999.755249.

de Ruijter, W. P., Ridderinkhof, H., Lutjeharms, J. R., Schouten, M. W., & Veth, C. (2002). Observations of the flow in the Mozambique Channel. Geophysical Research Letters, 29(10), 140-1. 10.1029/2001GL013714

Di Marco, S. F., Chapman, P., Nowlin Jr, W. D., Hacker, P., Donohue, K., Luther, M., ... & Toole, J. (2002). Volume transport and property distributions of the Mozambique Channel. Deep Sea Research Part II: Topical Studies in Oceanography, 49(7-8), 1481-1511. 10.1016.s-10967-0645(01)00159-X

Feuillet, N., Jorry, S., Crawford, W. C., Deplus, C., Thinon, I., Jacques, E., ... & Van der Woerd, J. (2021). Birth of a large volcanic edifice offshore Mayotte via lithosphere-scale dyke intrusion. Nature Geoscience, 14(10), 787-795. https://doi.org/10.31223/X5B89P

Fiedler, B., Fietzek, P., Vieira, N., Silva, P., Bittig, H. C., & Körtzinger, A. (2013). In situ CO2 and O2 measurements on a profiling float. Journal of atmospheric and oceanic technology, 30(1), 112-126. https://doi.org/10.1175/JTECH-D-12-00043.1

Fietzek, P., Fiedler, B., Steinhoff, T., & Körtzinger, A. (2014). In situ quality assessment of a novel underwater pCO2 sensor based on membrane equilibration and NDIR spectrometry. Journal of Atmospheric and Oceanic Technology, 31(1), 181-196. https://doi.org/10.1175/JTECH-D-13-00083.1

Francois, R. and Garrison, G. (1982). "Sound absorption based on ocean measurements: Part II: Boric acid contribution and equation for total absorption," Journal of the Acoustical Society of America, vol. 72, no. 6, pp. 1879-1890. https://doi.org/10.1121/1.388673.

Garau, B., Ruiz, S., Zhang, W. G., Pascual, A., Heslop, E., Kerfoot, J., & Tintoré, J. (2011). Thermal lag correction on Slocum CTD glider data. Journal of Atmospheric and Oceanic Technology, 28(9), 1065-1071. https://doi.org/10.1175/JTECH-D-10-05030.1

Garcia H.E., T.P. Boyer, O.K. Baranova, R.A. Locarnini, A.V. Mishonov, A. Grodsky, C.R. Paver, K.W. Weathers, I.V. Smolyar, J.R. Reagan, D. Seidov, M.M. Zweng (2019). DOI:10.13140/RG.2.2.34758.01602

Gentil, Mathieu & Many, Gaël & Durrieu de Madron, Xavier & Cauchy, Pierre & Pairaud, Ivane & Testor, Pierre & Verney, Romaric & Bourrin, François. (2020). Glider-Based Active Acoustic Monitoring of Currents and Turbidity in the Coastal Zone. Remote Sensing. 12. 10.3390/rs12182875.

I. Halo, B. Backeberg, P. Penven, I. Ansorge, C. Reason, J.E. Ullgren, Eddy properties in the Mozambique Channel: A comparison between observations and two numerical ocean circulation models, Deep Sea Research Part II: Topical Studies in Oceanography, Volume 100, 2014, Pages 38-53, ISSN 0967-0645, https://doi.org/10.1016/j.dsr2.2013.10.015.

Claudine Hauri, Brita Irving, Dan Hayes, Ehsan Abdi, Jöran Kemme, Nadja Kinski, and Andrew Michael Paul McDonnell, Expanding seawater carbon dioxide and methane measuring capabilities with a Seaglider, Preprint egusphere-2024-1055, https://doi.org/10.5194/egusphere-2024-1055

Hedgpeth, J.W. 1957 Treatise on marine ecology and paleoecology. Volume 1, Ecology. The Geological Society of America Memoir 67.

Heumann Alexandre, Margirier Félix, Rinnert Emmanuel, Lherminier Pascale, Scalabrin Carla, Geli Louis, Pasqueron De Fommervault Orens, Beguery Laurent (2024). 30 months data set of glider physico-chemical data off Mayotte Island near the Fani Maore volcano. SEANOE. https://doi.org/10.17882/99960

Intergovernmental Oceanographic Commission of UNESCO. 2013.Ocean Data Standards, Vol.3: Recommendation for a Quality Flag Scheme for the Exchange of Oceanographic and Marine Meteorological Data. (IOC Manuals and Guides, 54, Vol. 3.) 12 pp. (English.)(IOC/2013/MG/54-3). http://dx.doi.org/10.25607/OBP-6

Isabelle Leblond, Carla Scalabrin, Laurent Berger. Acoustic monitoring of gas emissions from the seafloor. Part I: quantifying the volumetric flow of bubbles. Mar Geophys Res (2014) 35:191–210. 10.1007/s11001-014-9223-y

Lemoine et al. (2020), The 2018–2019 seismo-volcanic crisis east of Mayotte, Comoros islands: seismicity and ground deformation markers of an exceptional submarine eruption, Geophys. J. Int., 223(1), 22–44, https://doi.org/10.1093/gji/ggaa273

Lopez-Garcia, P., Hull, T., Thomsen, S., Hahn, J., Queste, B. Y., Krahmann, G., Williams, C., Woo, M., Pattiaratchi, C., Coppola, L., Morales, T., Racapé, V., Gourcuff, C., Allen, J., Alou-Font, E., Zarokanellos, N., Turpin, V., Schmechtig, C., Testor, P., ..., Begler, C. (2022). OceanGliders Oxygen SOP [Guide]. OceanGliders. 10.25607/OBP-1756

Mastin Manon (2023). Fluid and gas emissions in a submarine eruption context offshore Mayotte Island : geochemical impact on the water column. PhD Thesis, Université de Bretagne Occidentale. https://theses.hal.science/tel-04394229

Manyilizu, M., Penven, P., & Reason, C. (2016). Annual cycle of the upper-ocean circulation and properties in the tropical western Indian Ocean. African Journal of Marine Science, 38(1), 81–99. https://doi.org/10.2989/1814232X.2016.1158123

Meurer, William & Blum, John & Shipman, Greg. (2021). Volumetric Mapping of Methane Concentrations at the Bush Hill Hydrocarbon Seep, Gulf of Mexico. Frontiers in Earth Science. 9. 10.3389/feart.2021.604930.

Miloshevich, L. M., Paukkunen, A., Vömel, H., & Oltmans, S. J. (2004). Development and validation of a time-lag correction for Vaisala radiosonde humidity measurements. Journal of Atmospheric and Oceanic Technology, 21(9), 1305-1327. https://doi.org/10.1175/1520-0426(2004)021<1305:DAVOAT>2.0.CO;2

Miramontes, E., Penven, P., Fierens, R., Droz, L., Toucanne, S., Jorry, S. J., ... & Raisson, F. (2019). The influence of bottom currents on the Zambezi Valley morphology (Mozambique Channel, SW Indian Ocean): In situ current observations and hydrodynamic modelling. Marine Geology, 410, 42-55 10.1016/j.margeo.2019.01.002

Morison, J., R. Andersen, N. Larson, E. D'Asaro, and T. Boyd, 1994: The correction for thermal-lag effects in Sea-Bird CTD data. J. Atmos. Oceanic Technol., 11, 1151–1164. https://doi.org/10.1175/1520-0426(1994)011<1151:TCFTLE>2.0.CO;2

Mullison, Jerry. (2017). Backscatter Estimation Using Broadband Acoustic Doppler Current Profilers-Updated.

Ronald S. Oremland, Barrie F. Taylor, Sulfate reduction and methanogenesis in marine sediments, Geochimica et Cosmochimica Acta, Volume 42, Issue 2, 1978, Pages 209-214, https://doi.org/10.1016/0016-7037(78)90133-3

Owens, W. B., & Millard Jr, R. C. (1985). A new algorithm for CTD oxygen calibration. Journal of Physical Oceanography, 15(5), 621-631.

Pasqueron de Fommervault, O. Besson, F., Lattes, P. (2018). SeaExplorer Underwater Glider: A New Tool to Measure WaterVelocity. Marine Technology 42, 44-47. 10.1109/OCEANSE.2019.8867228

Pouliquen Sylvie, Petit De La Villeon Loic, Carval Thierry (2011). Argo Data Management : contribution to Marine Climate Data System (MCDS) workshop . IDM/ISI/11-070 .

C. Schmechtig, V. Thierry, The Bio Argo Team Argo Quality Control Manual for Biogeochemical Data. The Bio Argo (2016), 10.13155/40879.

Stommel, H. 1989. The Slocum Mission. Oceanography 2(1):22–25, https://doi.org/10.5670/oceanog.1989.26.

Scalabrin Carla (2023). Site d'émissions de fluides, Mayotte, zone Fer à Cheval (C. Scalabrin, 2022). Ifremer GEO-OCEAN. https://doi.org//10.12770/070818f6-6520-49e4-bafd-9d4d0609bf7d

J.F. Ternon, P. Bach, R. Barlow, J. Huggett, S. Jaquemet, F. Marsac, F. Ménard, P. Penven, M. Potier, M.J. Roberts, The Mozambique Channel: From physics to upper trophic levels, Deep Sea Research Part II: Topical Studies in Oceanography, Volume 100, 2014, Pages 1-9, ISSN 0967-0645, https://doi.org/10.1016/j.dsr2.2013.10.012

Testor, Pierre & Meyers, Gary & Pattiaratchi, Charitha & Bachmayer, Ralf & Hayes, D. & Pouliquen, Sylvie & Villeon, Loic & Carval, Thierry & Ganachaud, Alexandre & Gourdeau, Lionel & Mortier, Laurent & Claustre, Hervé & Taillandier, Vincent & Lherminier, Pascale & Terre, T. & Visbeck, Martin & Karstensen, Johannes & Krahmann, Gerd & Alvarez, A. & Owens, Breck. (2010). Gliders as a Component of Future Observing Systems. Proceedings of OceanObs'09:Sustained Ocean. Observations and Information for Society .Hall, J., Harrison, D.E. & Stammer, D., Eds., ESA Publication WPP-306,. 2. 10.5270/OceanObs09.cwp.89

Gregor Rehder, Ira Leifer, Peter G. Brewer, Gernot Friederich, Edward T. Peltzer. Controls on methane bubble dissolution inside and outside the hydrate stability field from open ocean field experiments and numerical modeling. Marine Chemistry 114 (2009) 19–30 https://doi.org/10.1016/j.marchem.2009.03.004

Robert E. Todd, Francisco Chavez, Sophie Clayton, Sophie Cravatte, Marlos Goes, et al.. Global Perspectives on Observing Ocean Boundary Current Systems. Frontiers in Marine Science, Frontiers Media, 2019, 6, https://doi.org/10.3389/fmars.2019.00423

F. Roquet, G. Madec, Trevor J. McDougall, Paul M. Barker, Accurate polynomial expressions for the density and specific volume of seawater using the TEOS-10 standard, Ocean Modelling, Volume 90, 2015, Pages 29-43, ISSN 1463-5003, https://doi.org/10.1016/j.ocemod.2015.04.002

Russell-Cargill Louise M., Craddock Bradley S., Dinsdale Ross B., Doran Jacqueline G., Hunt Ben N., Hollings Ben (2018) Using autonomous underwater gliders for geochemical exploration surveys. The APPEA Journal 58, 367-380. https://doi.org/10.1071/AJ17079

Schott, F. A., S.-P. Xie, and J. P. McCreary Jr. (2009), Indian Ocean circulation and climate variability, Rev. Geophys., 47, RG1002, doi:10.1029/2007RG000245.

Van Haren, H., and L. Gostiaux (2010), A deep-ocean Kelvin-Helmholtz billow train, Geophys. Res. Lett., 37, L03605, doi:10.1029/2009GL041890.

Visbeck, M. (2002). Deep velocity profiling using lowered acoustic Doppler current profilers: Bottom track and inverse solutions. Journal of atmospheric and oceanic technology, 19(5), 794-807. https://doi.org/10.1175/1520-0426(2002)019<0794:DVPULA>2.0.CO;2

Wyrtki, K. (1971) Oceanographic Atlas of the International Indian Ocean Expedition. National Science Foundation, Washington DC.

Zinke et al. (2003), Postglacial flooding history of Mayotte Lagoon (Comoro Archipelago, southwest Indian Ocean). Marine Geology, 194(3–4), 181–196. https://doi.org/10.1016/s0025-3227(02)00705-3

Zinke et al. (2005), Facies and faunal assemblage changes in response to the Holocene transgression in the Holocene transgression in the Lagoon of Mayotte (Comoro Archipelago, SW Indian Ocean). Facies 50 :391–408 10.1007/s10347- 004-0040-7